

Stress state inferred from b-value and focal mechanism distributions in the aftershock area of the 2005 West Off Fukuoka Prefecture earthquake

Keita Chiba (✉ kchiba@sevo.kyushu-u.ac.jp)

Kyushu Daigaku <https://orcid.org/0000-0002-2841-3371>

Research Article

Keywords: b-value, Stress state, 2005 West Off Fukuoka Prefecture Earthquake, Focal mechanism, Stress tensor inversion

Posted Date: February 16th, 2021

DOI: <https://doi.org/10.21203/rs.3.rs-201023/v1>

License:  This work is licensed under a Creative Commons Attribution 4.0 International License.

[Read Full License](#)

Version of Record: A version of this preprint was published at Pure and Applied Geophysics on March 17th, 2021. See the published version at <https://doi.org/10.1007/s00024-021-02691-5>.

1 Submitted to *Pure and Applied Geophysics*

2

3 Stress state inferred from *b*-value and focal
4 mechanism distributions in the aftershock area of the
5 2005 West Off Fukuoka Prefecture earthquake

6

7 Keita Chiba^{1*}

8

9 Author#1: Keita Chiba, Institute of Seismology and Volcanology, Faculty of Science,

10 Kyushu University, 744 Motoooka, Nishi-Ku, Fukuoka, 819-0395 Japan,

11 kchiba@sevo.kyushu-u.ac.jp, Tel: +81 92-802-4346,

12 ORCID: <https://orcid.org/0000-0002-2841-3371>

13 *Corresponding author: Keita Chiba

14

15

16

17

18 *Abstract*—The spatiotemporal stress states in the aftershock region of the 2005 west off Fukuoka
19 prefecture earthquake are examined via an analysis of the b -values and focal mechanism solutions. The
20 aftershocks are aligned roughly NW–SE, with the southeastern part of the aftershock region believed to
21 correspond to Kego Fault, which extends beneath the Fukuoka metropolitan area. This study reveals
22 depth-dependent b -values in the focal region, where the b -values ($b = 0.7$ – 1.4) are generally higher above
23 the mainshock depth (9.5 km) and lower ($b = 0.5$ – 1.0) at greater depths. The shallower region possesses a
24 significant temporal increase in b -values, whereas a lateral b -value heterogeneity is observed in the
25 deeper region. The b -values ($b \sim 1.0$) near the mainshock are relatively high, whereas the northwestern
26 and southeastern edges of the deep region have lower b -values ($b = 0.5$ – 0.7). On the other hand, many of
27 the focal mechanisms for the $M \geq 3.5$ events are located in the low b -value area of the deep region. The
28 stress-tensor inversion results reveal a change in stress state from strike-slip to strike-slip/normal faulting.
29 These findings imply that the stress state remains high and/or slightly decreased in the northwestern and
30 southeastern parts of the deep region. These results and the findings of previous research on this
31 earthquake sequence suggest that the likelihood of future large earthquakes along the southeastern part of
32 the aftershock region should be considered relatively high.

33

34 **Keywords:** b -value, Stress state, 2005 West Off Fukuoka Prefecture Earthquake, Focal mechanism,
35 Stress tensor inversion

36

37 *1. Introduction*

38 The 2005 West Off Fukuoka Prefecture Earthquake (M_J 7.0) occurred in Genkai-nada,
39 Fukuoka Prefecture, northern Kyushu, Japan, on 20 March 2005 (e.g., Shimizu et al. 2006; Uehira et al.

40 2006). The hypocenter was located at 130.1616°E, 33.7434°N, and 9.5 km depth, with a best-fit focal
41 mechanism solution showing left-lateral strike slip with a tension axis aligned N23°W–S23°E (Uehira et
42 al. 2006). Many aftershocks occurred at 1–16 km depth, and were distributed along a 25-km-long NW–
43 SE-trending linear feature (Shimizu et al. 2006; Uehira et al. 2006). The largest aftershock (M_J 5.8)
44 occurred near the southeastern end of the aftershock region on 20 April 2005, followed by additional
45 aftershock activity to the southeast (e.g., Uehira et al. 2006). Numerous research studies have also
46 investigated the coseismic slip distribution of the mainshock, spatial distribution of static stress drops,
47 postseismic deformation, and attenuation structure in the focal region of the 2005 West Off Fukuoka
48 Prefecture Earthquake (e.g., Asano and Iwata 2006; Horikawa 2006; Iio et al. 2006; Matsumoto, S. et al.
49 2009; Nakao et al. 2006; Nishimura et al. 2006). Iio et al. (2006) have provided important details for
50 hazard assessments in the focal region via an investigation of the static stress drop distribution of the
51 aftershocks using the waveforms from temporary seismic stations; they highlighted the possibility of a
52 large stress concentration around the southeastern end of the aftershock area, which includes the largest
53 aftershock.

54 Many active faults exist in northern Kyushu district (The Research Group for Active Faults of
55 Japan 1991). The southeastern extension of the aftershock region is believed to correspond to the
56 northwestern edge of Kego Fault, which is known to be active fault (e.g., Okamura et al. 2009; Uehira et
57 al. 2006). Kego Fault runs beneath the Fukuoka metropolitan area, with a population of about 1.5 million.
58 Okamura et al. (2009) used acoustic exploration and sediment cores to investigate the paleoseismicity of
59 the Kego Fault and estimated that the latest two major earthquakes occurred 4,500–4,000 yBP and 8,500–
60 6,500 yBP, respectively. These short recurrence intervals are a stark contrast to the 15,500-year
61 recurrence interval estimated by Shimoyama et al. (2005). These geophysical and geological results

62 suggest that the next major earthquake might impact segments of Kego Fault that have not previously
63 ruptured, which run through the central part of Fukuoka City. The National Institute of Advanced
64 Industrial Science and Technology (AIST) (2005) calculated the Coulomb stress change induced by the
65 2005 mainshock, and found a positive stress change of up to 0.1–0.5 MPa around the southeastern and
66 northwestern ends of the aftershock area. The probability of a $M = 7.0$ earthquake in the next 30 years on
67 the Kego Fault (counted from 2005) increased about 7% due to the 2005 mainshock (AIST 2005). The
68 metropolitan area would be devastated if such a major earthquake were to occur. However, details of the
69 stress state have not been evaluated in and around the focal region, although the area remains seismically
70 active.

71 Here the b -values of the Gutenberg–Richter Law (Gutenberg and Richter 1944), which are
72 indicators of the stress state (e.g., Scholz 1968, 2015), are investigated in the aftershock region of the
73 2005 West Off Fukuoka Prefecture Earthquake using a seismic catalog that was compiled from data
74 recorded after the 2005 mainshock. Recently, the stress-dependent characteristics of the b -values were
75 used for real-time seismic hazard assessment. One of the main concerns after a large earthquake is
76 whether or not a stronger subsequent event will occur. Gulia and Wiemer (2019) examined time series of
77 b -values in many aftershock sequences, and found that a larger subsequent event is more likely to occur if
78 the b -value decreases substantially. Real-time monitoring of the b -value is thus considered useful to
79 estimate whether a larger subsequent event is likely. Furthermore, the focal mechanisms are inverted to
80 obtain the stress tensors and assess the present stress states in the study area. This inversion does not
81 determine the magnitude of the deviatoric stress at seismogenic depths (e.g. Gephart and Forsyth 1984;
82 Michael 1984, 1987). However, the orientation of the maximum horizontal stress axis relative to the fault
83 strike direction is useful to infer how the stress field evolves with time (e.g., Hardebeck and Hauksson

84 2001). The style of faulting, which depends on the directions of the principal stress axes, also indicates
85 the absolute stress level from the Coulomb failure criterion (e.g., Jaeger and Cook 1979). This study aims
86 to clarify the spatiotemporal stress states as well as resolve highly-stressed areas with high likelihoods of
87 nucleating large earthquakes in the focal region, through unified analysis of b -values and stress tensor
88 inversions.

89

90

91

2. Methods and data

92 2.1. b -values

93

The empirical relationship between the earthquake frequency and magnitude distribution,

94

which is known as the Gutenberg–Richter Law, is a power law of the form:

95

$$\log N = a - bM, \quad (1)$$

96

where $N(M)$ is the cumulative number of earthquakes with magnitude equal to or greater than M , and

97

a and b are constants (Ishimoto and Iida 1939, Gutenberg and Richter 1944). The constant b is termed

98

the b -value, and represents the ratio of small to large earthquakes. The b -value depends on various

99

factors, including the stress state, strength, material heterogeneity, and thermal gradient (e.g., Mogi 1962;

100

Scholz 1968, 2015; Warren and Latham 1970; Wyss 1973; Urbancic et al. 1992), and varies between 0.5

101

and 1.5 for different tectonic settings, with an average value of 1.0 (Frohlich and Davis 1993). The stress-

102

dependent characteristics of the b -values are among the most widely studied earthquake parameters in the

103

literature (e.g., Scholz 1968, 2015; Schorlemmer et al. 2004; Schorlemmer and Wiemer 2005). The

104 differential stress generally increases as the b -value decreases, and vice versa. Many studies have
105 examined the stress states in various tectonic settings using spatiotemporal b -value distributions (e.g.,
106 Chiba 2019, 2020; Ghosh et al. 2008; Nanjo and Yoshida 2018; Nanjo et al. 2016, 2019; Schorlemmer et
107 al. 2004; Schorlemmer and Wiemer 2005; Tormann et al. 2015). The highly stressed areas in any tectonic
108 setting, such as regions with a large coseismic slip and large slip deficit rate, are usually characterized by
109 low b -values. For example, Schorlemmer and Wiemer (2005) examined the b -value distributions in the
110 focal area prior to the 2004 M_w 6.0 Parkfield Earthquake on the San Andreas Fault (California, USA), and
111 found a close spatial correspondence between low b -values and large coseismic slip during the
112 mainshock. Ghosh et al. (2008) found a negative correlation between the b -value distribution and plate
113 locking inferred from geodetic estimates of interface locking along the Cocos Plate near Nicoya
114 Peninsula, Costa Rica. Nanjo et al. (2016) analyzed the b -value distribution in the focal region of the
115 2016 Kumamoto Earthquake, Japan, prior to the mainshock, and discovered that a zone near the
116 mainshock corresponds to a low b -value region. These examples verify that spatiotemporal b -value
117 analysis is an important and useful tool for seismic hazard assessment in regions with a high likelihood of
118 large earthquakes.

119

120 *2.2. b-value data and computational procedure*

121 The unified earthquake catalog maintained by the Japan Meteorological Agency (JMA
122 catalog) was used for the b -value calculations in this study, which included 15,381 events that were
123 recorded between 12:20 on 20 April 2005 (2005.3 in decimal year) to 23:59 on 31 January 2020 (JST) in
124 the region bounded by 130.0–130.5°E, 33.55–33.85°N, and 0.0–20.0 km depth. Data within one month of

125 the mainshock were excluded since the events recorded during this period were highly heterogeneous and
126 the JMA catalog was incomplete. Fig. 1 shows hypocenters of the $M \geq 0.5$ events; this choice of
127 magnitude threshold is explained below.

128 ZMAP (Wiemer 2001) was employed for the seismicity analysis of this dataset, including the
129 b -value computations. An estimation of the magnitude of completeness M_c , which is the minimum
130 magnitude in the earthquake catalog that satisfies the power law in Eq. (1), is crucial for the b -value
131 analysis. The detection limits of the JMA catalog have improved significantly since 2000; M_c is
132 typically 0.0–1.0 in Kyushu district (Nanjo et al. 2010). The maximum curvature method (Wiemer and
133 Wyss 2000) was employed to investigate temporal changes in M_c in the study area using overlapping
134 500-event windows and a 20-event step. Generally, $M_c < 0.5$ throughout the analysis period (Fig. 2a).
135 Gridding methods were further applied by calculating the spatial distribution of M_c using the maximum
136 curvature method (Wiemer and Wyss 2000). The M_c cross-section for events within 5 km of line A-B in
137 Fig. 1 was calculated using 0.5 km grid spacing and a constant sampling radius of 2.5 km, which
138 represents the optimal radius value for b -value computation of cross-sections, as explained below. M_c
139 varies across the study area, with $M_c \geq 0.5$ in the northwestern subregion (Fig. 2b). Two-step
140 screenings were therefore employed to choose M_c for the b -value calculations. First, a total of 9,324
141 $M \geq 0.5$ events were used for further analysis, selected based on spatiotemporal M_c distributions. Next,
142 local M_c values were recalculated at each grid point for $M \geq 0.5$ events, using this catalog and the
143 maximum curvature method (Wiemer and Wyss 2000); this was a precursory step to b -value calculations
144 due to observed spatial variations in M_c . Events with magnitudes below each new M_c value were
145 discarded. In addition, the maximum curvature method is known to often underestimate M_c by 0.2 on
146 average (Woessner and Wiemer 2005); therefore, an M_c correction of +0.2 was applied. The analysis

147 window was divided into two periods to investigate the temporal changes in b -values: the approximately
148 8-month period after the mainshock (period 1: 4335 events, 12:20 JST on 20 April 2005–31 December
149 2005) and the 2006–2020 period (period 2: 4989 events, 1 January 2006–31 January 2020). However, it is
150 insufficient to evaluate temporal changes in b -values using only arbitrarily-selected time windows. An
151 additional analysis, which divided the analysis window into three periods, was performed to investigate
152 the temporal changes in b -values in detail: period a1 was 12:20 JST on 20 April 2005–23:59 on 31
153 August 2005, and had 3298 events; period a2 was 1 September 2005–31 December 2007, with 3017
154 events; period a3 was 1 January 2008–31 January 2020, with 3009 events. This analysis was only used
155 for b -value calculations because there are too few available focal mechanisms to constrain stress tensor
156 inversions in three temporal subwindows.

157 Gridding methods were applied by calculating the maximum-likelihood b -values. Spatial b -
158 value distributions were constructed to produce plan-view maps and cross-sections using gridding
159 intervals of 0.005° and 0.5 km for the plan-view maps and cross-sections, respectively. Determining the
160 optimal sampling radii for the b -value calculations at each grid point is both necessary and non-trivial.
161 Fewer grid points match the required minimum number of events to constrain the b -values when the
162 sampling radii are small. Conversely, the resolution of the regional b -value heterogeneities is reduced
163 when the sampling radii are too large. The optimal sampling radius is the largest radius that still resolves
164 b -value heterogeneities in detail (Schorlemmer et al. 2004). The optimal sampling radius was determined
165 to be 2.5 km for the plan-view maps and cross-sections in this study after exploring a broad range of
166 sampling radii. The b -value was then calculated at each grid point via the maximum likelihood method
167 (Aki 1965):

168
$$b = \log e / (M_{mean} - M_0), \quad (2)$$

169 where M_{mean} is the mean magnitude and $M_0 = M_c - 0.05$ for uniform 0.1 magnitude bins. The
170 corresponding b -values were not calculated if a grid node had <50 events within a 2.5-km radius.

171 The heterogeneities in the b -value distributions were quantitatively evaluated using the p -test
172 (Utsu 1992), which is defined as:

$$173 \quad p = e^{(-dA/2-2)}, \quad (3)$$

174 where $dA = -2N\ln(N) + 2N_1\ln(N_1 + N_2b_1/b_2) + 2N_2\ln(N_1b_2/b_1 + N_2) - 2$, N_1 and N_2 are the
175 numbers of events within the volumes to be compared, and $N = N_1 + N_2$. Smaller p -values indicate
176 more significant b -value heterogeneities. Previous studies have found that b -value heterogeneity is
177 considered statistically significant if $\log p \leq -1.3$ ($p \leq 0.0498$) (Schorlemmer et al. 2004; Utsu 1992,
178 1999).

179

180 *2.3. Stress tensor inversion data and computational procedure*

181 The focal mechanisms that were used for the stress tensor inversion were estimated from F-
182 net data, which were recorded by the permanent seismic stations operated by the National Research
183 Institute for Earth Science and Disaster Resilience (NIED). Twenty-three focal mechanisms (13 events
184 during period 1 and 10 events during period 2), each with a variance reduction of >60% and trace data
185 from >3 stations, were inverted to determine the best-fitting normalized stress tensor for each period. The
186 stress tensor inversion was performed using the MSATSI software (Martinez-Garzon et al. 2014), a
187 MATLAB package based on Hardebeck and Michael (2006). This method uses the linearized inversion
188 scheme of Michael (1987), which is based on the Wallace-Bott hypothesis (Wallace 1951; Bott 1959),
189 whereby an earthquake slip's vector is parallel to the resolved shear stress on the fault plane, and a

190 damped inversion method is used to avoid the apparent spatial variability resulting from dividing the
191 analytical region into small subregions. The stress tensor inversion has four unknown parameters: the
192 three principal stress axes, $\sigma_1, \sigma_2, \sigma_3$, and the stress ratio:

$$193 \quad R = (\sigma_1 - \sigma_2)/(\sigma_1 - \sigma_3), \quad (4)$$

194 which represents the relative stress magnitude. The uncertainties in the results were evaluated via 500
195 bootstrap resamplings (Michael 1987). The number of events used to estimate the uncertainty in each
196 stress parameter was ≥ 20 in each trial. As mentioned in Section 2.2, stress tensor inversions were not
197 performed for each of the three temporal subwindows because there were too few available focal
198 mechanisms.

199

200 *3. Results*

201 The hypocenter distribution consists of a roughly NW–SE-oriented linear feature (Fig. 1).
202 There is no clear migration of events between periods 1 and 2. The b -value cross-sections are first
203 calculated for the events within 5.0 km of transect A–B in Fig. 1 during both analysis periods (Fig. 3)
204 based on the NW–SE alignment of the seismicity; this resolves depth-dependent characteristics with a
205 transition at the mainshock depth (9.5 km). The shallower region has relatively high b -values ($b = 0.7$ –
206 1.4) during both periods, whereas the b -values ($b = 0.5$ –1.0) are lower in the deeper region (Fig. 3). The
207 reduction in b -value ($b = 0.5$ –0.7) is especially significant in the northwestern and southeastern parts of
208 the deep region. Conversely, the characteristics of the b -values near the mainshock hypocenter differ
209 slightly from the overall feature. The b -values ($b \sim 1.0$) at 12.0–16.0 km depth (e.g., regions 1 and 5 in
210 Fig. 3) are higher than those ($b = 0.5$ –0.7) in the surrounding deeper region (e.g., regions 2 and 6) during

211 both periods; the b -values ($b \sim 0.7$) are relatively low at 6.0–10.0 km depth and near the mainshock
212 hypocenter (region 3) during period 1 compared to those ($b = 1.0$ – 1.4) in the surrounding shallow areas
213 (e.g., region 4); and the b -values increase ($b \sim 1.0$) in the areas near the mainshock (e.g., regions 5 and 7)
214 during period 2 (Fig. 3). Namely, low b -value areas at shallow depths near the mainshock are present
215 during period 1 but disappear during period 2. The observed spatial b -value heterogeneities for each
216 period are statistically significant at the 99% confidence level based on p -value tests (Utsu 1992), as
217 shown in Fig. 4.

218 Plan-view maps of the depth-dependent b -value characteristics are shown in Fig. 5 for the
219 shallow (0.0–9.5 km depth) and deep (9.5–20.0 km) regions during both periods, with the mainshock
220 depth serving as the transition between these two regions. The basic features are the same as those in the
221 cross-sections: the shallow region possesses relatively high b -values (Fig. 5a, c), whereas the b -values in
222 the deep region are low (Fig. 5b, d). This depth dependence is especially noticeable during period 2. The
223 b -values in the northwestern and southeastern parts of the aftershock region in the deep region are lower
224 than those near the mainshock (Fig. 5b, d). The b -values in the shallow region near the mainshock are
225 lower than those in the surrounding shallow area during period 1 (Fig. 5a). Noticeable temporal increases
226 in the b -values are also observed in the shallow region (Fig. 5a, c), whereas significant temporal
227 variations are not found at greater depths (Fig. 5b, d).

228 The differences in b -values between the two analyzed periods ($\Delta b = b_{period2} -$
229 $b_{period1}$) were calculated separately for the shallow and deep regions (Fig. 6a, c) to qualitatively evaluate
230 the temporal changes in b -values; the corresponding p -values indicate that these changes are statistically
231 significant. The b -values also exhibit statistically significant temporal increases ($p \leq 0.0498$) in many
232 parts of the shallow region, including the area near the mainshock (Fig. 6b). Areas with significant

233 temporal b -value changes are not widely distributed at greater depths (Fig. 6d).

234 Results for the three temporal subwindows indicate no clear migration of events between them
235 (Fig. S1). The general patterns in spatial and temporal distributions of b -values are the same as when the
236 analysis window is divided into two periods (Figs. S2–S4). However, using three subwindows captures
237 some temporal evolution of the b -values that was not clear when only two periods were used. The b -value
238 distributions in periods a1 and a3 are roughly similar to those of both subwindows in the two-period
239 analysis (Figs. 3, 5, S2, and S3); the b -value distribution for period a2 appears to show a transition
240 between periods 1 and 2. Most of the low b -values in the shallow region near the mainshock disappear
241 during period a2 (Figs. S2b and S3c). The observed low b -value anomaly may be characteristic of an
242 early stage during period 1. In addition, significant temporal increases in b -values between periods a1 and
243 a2 were found in many parts of the shallow region (Fig. S4a, b). b -values remained low at greater depths
244 during all three periods; areas with significant temporal b -value changes were not widely distributed (Fig.
245 S4c, d, g, h).

246 The relationship between the b -values and focal mechanisms was then investigated (Figs. 5
247 and S3). The focal mechanisms for the $M \geq 3.5$ events, which are relatively large earthquakes for the
248 analyzed region, were located in the low b -value ($b = 0.5$ – 0.7) area of the deep region; this finding is
249 consistent with the definition of the b -value that moderate to large earthquakes are likely to occur in
250 regions with low b -value. A stress tensor inversion was performed for each period using these focal
251 mechanisms. The stress state obtained for period 1 was dominated by strike-slip fault type (Fig. 7), with
252 $R = 0.51$ and a E–W-oriented maximum principal stress. A counterclockwise rotation of the maximum
253 principal stress and changes in the stress ratio were determined for period 2, with a decrease in the stress
254 ratio to $R = 0.29$ and a ENE–WSW-oriented maximum principal stress. The rotation of the maximum

255 principal stress was statistically significant at the 95% confidence level. This relatively low stress ratio
256 represents a stress state that is indicative of strike-slip/normal faulting (Fig. 7). This observation implies
257 that the stress state changed at greater depths, even though there were no significant temporal changes in
258 *b*-values.

259

260

4. Discussion

261 The spatiotemporal *b*-value distributions are highly heterogeneous in the aftershock region of
262 the 2005 West Off Fukuoka Prefecture Earthquake, with the stress-tensor inversion results indicating that
263 the stress state below 9.5 km depth changed from a strike-slip-dominated to strike-slip/normal faulting
264 regime. These results imply that the stress state is heterogeneous across the study area. Possible causes of
265 the observed stress heterogeneity in the analyzed region are discussed in this section by comparing the
266 results obtained in this study with those from previous studies. The areas with a high likelihood of
267 nucleating large earthquakes are also evaluated.

268 The key seismic characteristics found in this study include the overall depth-dependence of
269 the *b*-value distributions. The shallow region possesses relatively high *b*-values, whereas the *b*-values in
270 the deep region are low (Figs. 3 and 5). Uehira et al. (2006) reported that the aftershock distribution in the
271 central part of the study area was aligned on different fault planes that split at the mainshock depth, with a
272 difference of $\sim 10^\circ$ between their respective strikes and dips. Furthermore, they noticed that the mainshock
273 focal mechanism estimated from *P*-wave first-motion polarities was consistent with the deeper fault
274 plane, whereas the moment tensor solution estimated from broadband seismic waveform data
275 (Matsumoto, T. et al. 2006) was consistent with the shallower fault plane. The large coseismic slip of the

276 mainshock was mainly observed in the southeastern part of the aftershock region, near the mainshock, at
277 shallower depths (e.g., Asano and Iwata 2006; Horikawa 2006). Uehira et al. (2006) suggested that the
278 mainshock rupture initiated at the hypocenter and propagated downward, then ruptured the lower plane
279 and propagated upward, with this last rupture segment releasing most of the associated seismic moment.
280 These findings suggest that more accumulated stress was released at shallower depths. The high b -values
281 in the shallow region can therefore be interpreted as a low-stress state associated with significant stress
282 release due to large coseismic slip. Nakao et al. (2006) found notable postseismic deformation on the
283 coseismic fault at <3.0 km depth, with the postseismic slip on the fault accounting for up to ~13% of the
284 coseismic slip. The b -values in the shallow region are especially high in the uppermost layers of Fig. 3.
285 These findings are all consistent with a low-stress state in the shallow region.

286 A comparison of the presented results with a b -value analysis in the focal region of the 2016
287 Kumamoto Earthquake is useful for understanding the potential causes of the b -value heterogeneities
288 found in this study. The 16 April 2016 M_J 7.3 Kumamoto Earthquake occurred in the Futagawa-Hinagu
289 fault zone, Kumamoto Prefecture, central Kyusyu, Japan. Nanjo et al. (2019) analyzed the b -value
290 distribution after the mainshock in the focal region, and found a highly stressed area with low b -values at
291 the southern end of the causative faults. Their interpretation was that the heterogeneous b -values in the
292 focal region were due to postseismic deformation. The focal region was located at the boundary between
293 an afterslip-dominated region and viscoelastic deformation-dominated region (Nanjo et al. 2019). They
294 suggested that there was a local increase in the stresses at the boundary between regimes dominated by
295 different postseismic deformation processes based on the aftershock decay law of Utsu (1961) and a
296 seismicity rate model inferred from the stressing history (Dieterich 1994). Compared with the Kumamoto
297 earthquake, the postseismic deformation associated with the Fukuoka earthquake was restricted to very

298 shallow depths in the focal region (e.g., Nakao et al. 2006). The significant temporal changes in b -values
299 in the present study are mainly found in the shallow region, where afterslip occurred. Nakao et al. (2006)
300 detected postseismic deformation using GPS time-series data from 21 March to 27 June 2005. Significant
301 postseismic deformation was clearly seen around the aftershock area during the analysis period of the
302 present study (after 2005-04-20). In addition, the Geospatial Information Authority of Japan (GSI) (2006)
303 reported that postseismic deformation ended in November 2005. These observations imply that
304 significant postseismic deformation occurred during the early stage of period 1, which approximately
305 corresponds to period a1 (2005-04-20–2005-08-31) in the three-subwindow analysis of the present study.
306 Evidently, significant temporal increases in b -values between periods a1 and a2 were observable in many
307 parts of the shallow region (Fig. S4a, b). Therefore, the postseismic deformation following a mainshock
308 may play an important role in the temporal evolution of the b -values. Furthermore, the increase in b -
309 values near the mainshock in the shallow region, which approximately corresponds to regions 3 and 7 in
310 Fig. 3, may also be ascribed to a decrease in the effective normal stress due to increased pore fluid
311 pressure, which will be discussed below. These findings indicate that it is unlikely that the shallow region
312 is the potential location of another large earthquake in the near future since a significant amount of stress
313 was released by coseismic and postseismic slip.

314 The heterogeneity of the b -value distribution in the deeper region is then discussed. The
315 southeastern extension of the aftershock region appears to correspond to the northwestern edge of Kego
316 Fault, which extends beneath the Fukuoka metropolitan area (e.g., Okamura et al. 2009; Uehira et al.
317 2006). An evaluation of the stress state in the deeper region is therefore considered crucial for the
318 assessment of possible large earthquakes in the future. Matsumoto, S. et al. (2009) investigated the
319 seismic-wave attenuation (Q^{-1}) structure in and around the aftershock region of the 2005 mainshock, and

320 discovered a highly heterogeneous Q^{-1} structure in the focal region. Areas with large slip and high
321 aftershock activity were located in low Q^{-1} regions, whereas high a Q^{-1} region was found along the
322 southeastern edge of the aftershock region, near the largest aftershock. Matsumoto, S. et al. (2009)
323 suggested that the low and high Q^{-1} regions corresponded to relatively high and low fault strengths,
324 respectively. The largest aftershock has the same strike angle as Kego Fault (Uehira et al. 2006).
325 Matsumoto, S. et al. (2009) posited a segment boundary between the mainshock fault and Kego Fault,
326 where the fault strength is weak, based on the difference between the strike angles of the mainshock and
327 largest aftershock. Iio et al. (2006) investigated the spatial distribution of the static stress drops of the
328 Fukuoka earthquake aftershocks from 23 March to 31 May 2005, and suggested the possibility of more
329 stress being concentrated along the southeastern edge of the aftershock region. The b -values along the
330 southeastern edge of the deeper region are consistent with the results of Iio et al. (2006), and were low
331 throughout the entire analysis period (Figs. 3 and 5). These findings suggest that the southeastern extent
332 of the aftershock region, including the largest aftershock, comprises a highly stressed area with a
333 relatively low fault strength. This area may therefore have a high probability of experiencing a large
334 earthquake in the future compared to northwestern part of the aftershock region, even though both
335 subregions have low b -values. The potential causes of the relatively high b -values below the mainshock
336 are considered based on the findings of other geophysical studies. Wang and Zhao (2006) investigated the
337 3-D seismic velocity and Poisson's ratio structures in the epicentral area of the 2005 mainshock and
338 found that the mainshock was located at the boundary between high- and low-velocity regions in the
339 upper crust, with the lower crust side corresponding to a low-velocity, high Poisson's ratio region. They
340 interpreted the low-velocity region beneath the mainshock to possess fluids associated with mantle
341 upwelling due to the opening of Okinawa Trough. This finding suggests that fluids in and around a

342 mainshock source area may play an important role in earthquake generation (Wang and Zhao 2006). The
343 relatively high b -values in the region beneath the mainshock are therefore considered to be generated by a
344 reduction in the effective normal stress due to abundant fluids in the focal region. The geophysical
345 interpretation of Wang and Zhao (2006) is helpful for inferring the cause of the temporal increase in b -
346 values in the shallow region near the mainshock (regions 3 and 7 in Fig. 3). Fluid injection from the
347 deeper region may continue if this increase in b -values occurs due to an increase in pore pressure related
348 to the fluids beneath the focal region.

349 Most of the focal mechanisms included in the stress tensor inversion were located in the
350 northwestern and southeastern parts of the aftershock region, which possess low b -value areas in the
351 deeper region (Fig. 5). Unfortunately, the data are too sparse to invert for a stress tensor at each edge
352 since only 13 and 10 events were available for periods 1 and 2, respectively. It should therefore be noted
353 that the results of the stress tensor inversion show average stress states in both the deep northwestern and
354 southeastern subregions during each period; despite this limitation, the inversion results revealed a change
355 in the stress field that was characterized by counterclockwise rotation of the maximum principal stress
356 axis and a change in R from strike-slip to strike-slip/normal faulting. This change in R is useful to infer
357 the differential stress near both edges of the aftershock region. The Coulomb failure criterion states that
358 normal faulting events sustain the lowest differential stresses, strike-slip events are intermediate, and
359 reverse faulting events have the highest stresses, assuming that the vertical stress is equal to the
360 overburden pressure (e.g., Jaeger and Cook 1979). The observed change in R implies that the average
361 differential stress decreased slightly in these subregions during the study period. Areas with the low b -
362 values appeared to decrease further during period 2 based on the b -value cross-sections and plan-view
363 maps (Figs. 3b and 6c, respectively), although the decreases in the low b -value areas were not necessarily

364 statistically significant at many nodes (Fig. 6d). The angle between the strike of the fault plane and
365 maximum principal stress axis direction is used to infer the shear strength in the focal region (e.g.,
366 Hardebeck and Hauksson 2001). The maximum principal stress axis direction should be aligned $\sim 30^\circ$
367 relative to the fault plane for a strong fault, which is controlled by the frictional force (Byerlee 1978). On
368 the other hand, if the fault is weak, then the direction is predicted to be at a higher angle. The hypocenter
369 distribution consists of a roughly NW–SE-oriented linear feature (Fig. 1). Therefore, the angle of σ_1
370 relative to the mainshock fault strike was rotated, and increased, from period 1 to period 2 (Figs. 7a, c).
371 This finding also supports the observation of a slight decrease in average differential stress.

372 The potential cause of the slight decrease in the differential stress in the region with low b -
373 values is unknown because no significant postseismic deformation was observed in the deeper region
374 (Nakao et al. 2006). However, a region with significant low b -values does not necessarily lead to a future
375 large earthquake. For example, Tormann et al. (2015) analyzed the b -values along the subducting Pacific
376 Plate off Japan over a period that included the 2003 M_w 8.3 Tokachi-oki and 2011 M_w 9.0 Tohoku-oki
377 earthquakes, and found that the former occurred within an area of persistent low b -values off Hokkaido,
378 but not in a region of significant low b -values. On the other hand, the latter occurred within a subregion
379 of distinct low b -values in the subsequent high-slip area of the mainshock (Tormann et al. 2015). The
380 causes of these b -value differences remain unknown. Whether a significant decrease in b -value prior to a
381 major earthquake is an ubiquitous phenomenon is a question that should be approached with caution, as
382 some previous studies of major earthquakes found precursory increases in b -values (e.g., Smith 1981).
383 This point will be addressed in future research, where it can be considered in the context of other
384 geophysical studies. It is noteworthy, however, that El-Isa and Eaton (2014) reviewed previous research
385 on spatial and temporal variations in b -values and found that the vast majority of previous papers support

386 a decrease in b -value before a major earthquake. A significant and/or moderate decrease in b -value is
387 therefore useful information when drawing inferences about stress accumulation. Here the deeper region
388 along the southeastern edge of the aftershock region is considered to have a high likelihood of triggering
389 future large earthquakes due to the low b -values; however, there is a possibility that the differential stress
390 decreased slightly in the focal region. Temporal changes in the b -values that were related to the presence
391 of fluids were also found near the mainshock hypocenter. An increase in b -values related to a reduction in
392 effective stress, which is due to the presence of abundant fluids, may also be an important precursor to the
393 next large earthquake. Wiemer et al. (1998) reported that increased pore pressure lowered effective stress
394 and increased b -value, a phenomenon associated with the onset of an earthquake swarm at Long Valley
395 Caldera, California. The possibility that seismic activity increases due to abundant fluids in the focal
396 region cannot be ruled out.

397

398 *5. Conclusions*

399 This study examined the spatiotemporal b -value distributions in the aftershock region of the
400 2005 West Off Fukuoka Prefecture Earthquake. The b -value distributions possess distinct depth-
401 dependent characteristics, with the mainshock depth forming the transition zone. Relatively high b -values
402 ($b = 0.7\text{--}1.4$) are distributed throughout the shallow region, whereas the b -values ($b = 0.5\text{--}1.0$) in the
403 deep region are low. The high b -values in the shallow region are ascribed to significant stress release due
404 to large coseismic and postseismic slip. Although the b -values are generally low in the deep region, the
405 area below the mainshock possesses relatively high b -values ($b \sim 1.0$). This anomaly may reflect a
406 decrease in the effective stress due to an increase in pore fluid pressure that is caused by abundant fluids

407 in the focal region. The b -values ($b = 0.5\text{--}0.7$) below 9.5 km depth in the northwestern and southeastern
408 parts of the aftershock region remained low throughout the analysis period, although a stress tensor
409 inversion using focal mechanisms revealed a slight decrease in the average differential stress in these
410 areas. It is possible that the southeastern part of the aftershock region possesses a high likelihood of
411 hosting future large earthquakes.

412

413 *Acknowledgments*

414 The author used data from the Japan Meteorological Agency (JMA) unified earthquake catalog (<https://www.data.jma.go.jp/svd/eqev/data/bulletin/index.html>). The ZMAP MATLAB software package
415 (http://www.seismo.ethz.ch/static/stat_2010_website/stat-website-pre2010/www.earthquake.ethz.ch/software/zmap.html) was used for the b -value analysis. The figures were prepared
416 using the Generic Mapping Tools software package (Wessel et al. 2013). This study was partially
417 funded by Tokio Marine Kagami Memorial Foundation, Japan (EAKF320500). The author
418 thanks the editor Carla Braitenberg and two anonymous reviewers for helping to improve the
419 manuscript.

422

423 REFERENCES

- 424 Aki, K. (1965). Maximum likelihood estimate of b in the formula $\log N = a - bM$ and its confidence
425 limits. *Bulletin of Earthquake Research Institute of the University of Tokyo*, 43, 237–239.
- 426 Asano, K., & Iwata, T. (2006). Source process and near-source ground motions of the 2005 West Off
427 Fukuoka Prefecture Earthquake. *Earth, Planets and Space*, 58(1), 93-98.

- 428 Bott, M. H. P. (1959). The mechanics of oblique slip faulting. *Geological Magazine*, 96, 109-117.
- 429 Byerlee, J. (1978). Friction of rock. *Pure and Applied Geophysics*, 116, 615–4626.
- 430 Chiba, K. (2019). Spatial and temporal distributions of b-values related to long-term slow-slip and low-
431 frequency earthquakes in the Bungo Channel and Hyuga-nada regions, Japan. *Tectonophysics*, 757, 1-
432 9. <https://doi.org/10.1016/j.tecto.2019.02.021>.
- 433 Chiba, K. (2020). Stress state along the western Nankai Trough subduction zone inferred from *b*-values,
434 long-term slow slip events, and low frequency earthquakes. *Earth, Planets and Space*, 72(3).
435 <https://doi.org/10.1186/s40623-020-1130-7>.
- 436 Dieterich, J. (1994). A constitutive law for rate of earthquake production and its application to earthquake
437 clustering. *Journal of Geophysical Research*, 99(B2), 2601-2618. <https://doi.org/10.1029/93JB02581>.
- 438 El-Isa, Z.H. & Eaton, D.W. (2014). Spatiotemporal variations in the *b*-value of earthquake magnitude-
439 frequency distributions: Classification and causes. *Tectonophysics*, 615-616, 1-11.
440 <https://doi.org/10.1016/j.tecto.2013.12.001>.
- 441 Frohlich, C., & Davis, S. (1993). Teleseismic b values; or, much ado about 1.0. *Journal of Geophysical*
442 *Research*, 98(B1), 631-644.
- 443 Geospatial Information Authority of Japan. (2006). Crustal deformation and a fault mode of the West –
444 off Fukuoka Prefecture Earthquake in 2005. <https://www.gsi.go.jp/common/000025591.pdf> (in
445 Japanese).
- 446 Gephart, J. W., & Forsyth, D. W. (1984). An improved method for determining the regional stress tensor
447 using earthquake focal mechanism data: Application to the San Fernando earthquake sequence.
448 *Journal of Geophysical Research*, 89, 9,305-9,320.
- 449 Ghosh, A., Newman, A.V., Thomas, A.M., & Farmer, G.T. (2008). Interface locking along the

450 subduction megathrust from *b*-value mapping near Nicoya Peninsula, Costa Rica. *Geophysical*
451 *Research Letters*, 35, L01301. <https://doi.org/10.1029/2007GL031617>.

452 Gulia, L., & Wiemer, S. (2019). Real-time discrimination of earthquake foreshocks and aftershocks.
453 *Nature*, 574, 193-199. <https://doi.org/10.1038/s41586-019-1606-4>.

454 Gutenberg, B., & Richter, C. F. (1944). Frequency of earthquakes in California. *Bulletin of the*
455 *Seismological Society of America*, 34, 185-188.

456 Hardebeck, J.L., & Hauksson, E. (2001). Crustal stress field in southern California and its implications
457 for fault mechanics. *Journal of Geophysical Research*, 106(B10), 21,859-21.882.

458 Hardebeck, J. L., & Michael, A. J. (2006). Damped regional-scale stress inversions: Methodology and
459 examples for southern California and the Coalinga aftershock sequence. *Journal of Geophysical*
460 *Research*, 111, B11310. <https://doi.org/10.1029/2005JB004144>.

461 Horikawa, H. (2006). Rupture process of the 2005 West Off Fukuoka Prefecture, Japan, earthquake.
462 *Earth, Planets and Space*, 58, 87-92.

463 Iio, Y., Katao, H., Ueno, T., Enescu, B., Hirano, N., Okada, T., Uchida, N., Matsumoto, S., Matsuhima, T.,
464 Uehira, K., & Shimizu, H. (2006). Spatial distribution of seismic stress drops for aftershocks of the
465 2005 West Off Fukuoka Prefecture Earthquake. *Earth, Planets and Space*, 58, 1611-1615.

466 Ishimoto, M., & Iida, K. (1939). Observations sur les seisms enregistré par le microseismograph construit
467 demiemment. *Bulletin of the Earthquake Research Institute, Tokyo Imperial University*, 17, 443–478.

468 Jaeger, J., & Cook, N.G.W. (1979). *Fundamental of Rock Mechanics*, 3rd ed, Chapman and Hall,
469 London.

470 Martinez-Garzon, P., Kwiatek, G., Ickrath, M., & Bohnhoff, M. (2014). MSATSI: A MATLAB package
471 for stress inversion combining solid classic methodology, a new simplified user-handling and a

472 visualization tool. *Seismological Research Letters*, 85(4). <https://doi.org/10.1785/0220130189>.

473 Matsumoto, S., Uehira, K., Watanabe, A., Goto, K., Iio, Y., Hirata, N., Okada, T., Takahashi, H.,
474 Shimizu, H., Shinohara, M., & Kanazawa, T. (2009). High resolution Q^{-1} estimation based on
475 extension of coda normalization method and its application to P -wave attenuation structure in the
476 aftershock area of the 2005 West Off Fukuoka Prefecture Earthquake (M 7.0). *Geophysical Journal*
477 *International*, 179, 1039-1054. <https://doi.org/10.1111/j.1365-246X.2009.04313.x>.

478 Matsumoto, T., Ito, Y., Matsubayashi, H., & Sekiguchi, S. (2006). Spatial distribution of F-net moment
479 tensors of the 2005 West Off Fukuoka Prefecture Earthquake determined by the extended method of
480 the NIED F-Net routine. *Earth Planets Space*, 58, 63-67.

481 Michael, A. J. (1984). Determination of stress from slip data: Faults and folds. *Journal of Geophysical*
482 *Research*, 89, 11,517-11,526.

483 Michael, A.J. (1987). Stress rotation during the Coalinga aftershock sequence. *Journal of Geophysical*
484 *Research*, 92, 7,963-7,979.

485 Mogi, K. (1962). Magnitude-Frequency relation for elastic shocks accompanying fractures of various
486 materials and some related problems in earthquakes. *Bulletin of the Earthquake Research Institute*,
487 *University of Tokyo*, 40, 831–853.

488 Nakao, S., Takahashi, H., Matsushima, T., Kohno, Y., & Ichiyanagi, M. (2006). Postseismic deformation
489 following the 2005 West Off Fukuoka Prefecture Earthquake (M 7.0) derived by GPS observation.
490 *Earth Planets Space*, 58, 1617-1620.

491 Nanjo, K. Z., Ishibe, T., Tsuruoka, D., Schorlemmer, D., Ishigaki, Y., & Hirata, N. (2010). Analysis of
492 the Completeness Magnitude and Seismic Network Coverage of Japan. *Bulletin of the Seismological*
493 *Society of America*, 100(6), 3261-3268. <https://doi.org/10.1785/0120100077>.

494 Nanjo, K. Z., Izutsu, J., Orihara, Y., Furuse, N., Togo, S., Nitta, H., Okada, T., Tanaka, R., Kamogawa,
495 M., & Nagao, T. (2016). Seismicity prior to the 2016 Kumamoto earthquakes. *Earth, Planets and*
496 *Space*, 68, 187. <https://doi.org/10.1186/s40623-016-0558-2>.

497 Nanjo, K.Z., & Yoshida, A. (2018). A b map implying the first eastern rupture of the Nankai Trough
498 earthquakes. *Nature Communications*, 9, 1117. <https://doi.org/10.1038/s41467-018-03514-3>.

499 Nanjo, K.Z., Izutsu, J., Orihara, Y., Kamogawa, Y., & Nagano, T. (2019). Changes in seismicity pattern
500 due to the 2016 Kumamoto Earthquakes identify a highly stressed area on the Hinagu fault zone.
501 *Geophysical Research Letters*, 46(16). <https://doi.org/10.1029/2019GL083463>.

502 National Institute of Advanced Industrial Science and Technology. (2005). Change in future
503 earthquake probability due to fault interaction. [https://www.aist.go.jp/Portals/0/resource_images/
504 aist_j/aistinfo/aist_today/vol05_05/vol05_05_p14_15.pdf](https://www.aist.go.jp/Portals/0/resource_images/aist_j/aistinfo/aist_today/vol05_05/vol05_05_p14_15.pdf) (in Japanese).

505 Nishimura, T., Fujiwara, S., Murakami, M., Suito, H., Tobita, M., & Yagai, H. (2006). Fault model of the
506 2005 Fukuoka-ken Seiho-oki earthquake estimated from coseismic deformation observed by GPS and
507 InSAR. *Earth, Planets and Space*, 58, 51-56.

508 Okamura, M., Matsuoka, H., Nakashima, T., Nakata, T., Chida, N., Hirata, K., & Shimazaki, K. (2009).
509 Holocene Paleoseismicity on Kego Fault in Hakata Bay, Northern Kyushu, Japan. *Zisin*, 2(61), 175-
510 190. (in Japanese).

511 Scholz, C. H. (1968). The frequency-magnitude relation of microfracturing in rock and its relation to
512 earthquakes. *Bulletin of the Seismological Society of America*, 58, 399–415.

513 Scholz, C. H. (2015). On the stress dependence of the earthquake b value. *Geophysical Research Letters*,
514 42, 1399–1402. <https://doi.org/10.1002/2014GL062863>.

515 Schorlemmer, D., Wiemer, S., & Wyss, M. (2004). Earthquake statistics at Parkfield: 1. Stationarity of b

516 values. *Journal of Geophysical Research*, 109, B12307. <https://doi.org/10.1029/2004JB003234>.

517 Schorlemmer, D., & Wiemer, S. (2005). Microseismicity data forecast rupture area. *Nature*, 434, 1086.

518 <https://doi.org/10.1038/4341086a>.

519 Shimizu, H., Takahashi, T., Okada, T., Kanazawa, T., Iio, Y., Miyamachi, H., Matsushima, T.,

520 Ichiyangi, N., Uchida, N., Iwasaki, T., Katao, H., Goto, K., Matsumoto, S., Hirata, N., Nakao, S.,

521 Uehira, K., Shinohara, M., Yakiwara, H., Kame, T., Urabe, T., Matsuwo, N., Yamada, T., Watanabe,

522 A., Nakahigashi, K., Enescu, B., Uchida, K., Hashimoto, S., Hirano, S., Yagi, T., Kohno, Y., Ueno,

523 T., Saito, M., & Hori, M (2006). Aftershock seismicity and fault structure of the 2005 West Off

524 Fukuoka Prefecture Earthquake (M_{JMA} 7.0) derived from urgent joint observations. *Earth, Planets and*

525 *Space*, 58, 1599-1604.

526 Shimoyama, S., Iso, N., Matsuda, T., Ichihara, T., Chida, N., Okamura, M., Mogi, T., Suzuki, S., Ochiai,

527 H., Nagasawa, S., Imanishi, H., Kawabata, F., Yakabe, H., Ooteki, M., & Matsuura, K. (2005).

528 Trenching study at Yaukuin site across the Kego fault, Fukuoka City, West Japan. *Active Fault*

529 *Research*, 25, 117-128.

530 Smith, W.D. (1981). The b-value as an earthquake precursor, *Nature*, 289, 136-139.

531 <https://doi.org/10.1038/289136a0>.

532 The Research Group for Active Faults of Japan. (1991). *Active Faults in Japan* (revised edition), 488 pp,

533 *University of Tokyo Press*, (in Japanese).

534 Tormann, T., Enescu, B., Woessener, J., & Wiemer, S. (2015). Randomness of megathrust earthquakes

535 implied by rapid stress recovery after the Japan earthquake. *Nature Geoscience*, 8(2), 152-158.

536 <https://doi.org/10.1038/ngeo2343>.

537 Uehira et al. (2006). Precise aftershock distribution of the 2005 West Off Fukuoka Prefecture Earthquake

538 (M_j = 7.0) by using a dense onshore and offshore seismic network. *Earth, Planets and Space*, 58,
539 1605-1610.

540 Urbancic, T.I., Trifu, C. I., Long, J. M., & Young, R. P. (1992). Space-time correlations of b values with
541 stress release. *Pure and Applied Geophysics*, 139(3), 449–462.

542 Utsu, T. (1961). A statistical study on the occurrence of aftershocks. *Geophysics*, 30. 521-605.

543 Utsu, T. (1992). On seismicity, in: Report of Cooperative Research of the Institute of Statistical
544 Mathematics. *The Institute of Statistical Mathematics Tokyo*, 34, 139–157.

545 Utsu, T. (1999). Representation and analysis of the earthquake size distribution: A historical review and
546 some approaches. *Pure and Applied Geophysics*, 155, 509-535.

547 Wallace, R. E. (1951). Geometry of shearing stress and relationship to faulting. *The Journal of Geology*,
548 59, 111-130.

549 Wang, Z., & Zhao, D. (2006). Seismic evidence for the influence of fluids on the 2005 west off Fukuoka
550 prefecture earthquake in southwest Japan. *Physics of the Earth and Planetary Interiors*, 155, 313-324.

551 Warren, N. W., & Latham, G. V. (1970). An experimental study of thermally induced microfracturing
552 and its relation to volcanic seismicity. *Journal of Geophysical Research*, 75, 4455–4464.
553 <https://doi.org/10.1029/JB075i023p04455>.

554 Wessel, P., Smith, W. H. F., Scharroo, R. R., Luis, J. F., & Wobbe, F. (2013). Generic Mapping Tools:
555 improved version released. *Eos, Transactions American Geophysical Union*, 94, 409-410.
556 <https://doi.org/10.1002/2013EO450001>.

557 Wiemer, S. (2001). A software package to analyze seismicity: ZMAP. *Seismological Research Letters*,
558 72(3), 373–382.

559 Wiemer, S., & Wyss, M. (2000). Minimum magnitude of completeness in earthquake catalogs: examples

560 from Alaska, the Western United States, and Japan. *Bulletin of the Seismological Society of America*,
561 90, 859–869.

562 Wiemer, S., McNutt, S.R., & Wyss, M. (1998). Temporal and three-dimensional spatial analyses of the
563 frequency-magnitude distribution near Long Valley Caldera, California. *Geophysical Journal*
564 *International*, 134, 409–421. <https://doi.org/10.1406/j.1365-246x.1998.00561.x>.

565 Woessner, J., & Wiemer, S. (2005). Assessing the quality of earthquake catalogues: estimating the
566 magnitude of completeness and its uncertainty. *Bulletin of the Seismological Society of America*,
567 95(2), 684–498. <https://doi.org/10.1785/0120040007>.

568 Wyss, M. (1973). Towards a physical understanding of the earthquake frequency distribution.
569 *Geophysical Journal of the Royal Astronomical Society*, 31, 341–359. [https://doi.org/10.1111/j.1365-](https://doi.org/10.1111/j.1365-246X.1973.tb06506.x)
570 [246X.1973.tb06506.x](https://doi.org/10.1111/j.1365-246X.1973.tb06506.x).
571

572

Figure Captions

573

574

Figure 1

575 Left: Epicentral distribution of the $M \geq 0.5$ earthquakes. The red and green circles represent the period 1,

576 (12:20 JST on 20 April 2005 to 23:59 on 31 December 2005) and period 2 (00:00 JST on 1 January 2006

577 to 23:59 on 31 January 2020) events, respectively. The events are scaled by their magnitudes. The yellow

578 and blue stars represent the hypocenters of the mainshock and largest aftershock (M_J 5.8, 06:11 JST on 20

579 April 2005), respectively. The yellow and blue focal mechanisms are those for the mainshock and largest

580 aftershock, respectively. The red lines indicate active faults (The Research Group for Active Faults of

581 Japan 1991). Line A–B shows the location of the b -value cross-section in Fig. 3. The red rectangle

582 represents the region used for b -value analysis in Figs. 5 and 6. The inset map shows the analyzed region

583 with respect to western Japan. Right: Cross-section of the hypocenters within 5 km of A–B.

584

585

Figure 2

586 (a) M_c as a function of time in the area bordered by the red rectangle in Fig. 1. The dashed gray lines

587 represent the standard deviation of the calculated M_c values. The maximum curvature method (Wiemer

588 and Wyss 2000) was employed to investigate the M_c distribution in the study area using overlapping

589 500-event windows and a 20-event step. (b) Spatial distribution of M_c estimated using the maximum

590 curvature method (Wiemer and Wyss 2000) with 0.5 km grid spacing and a constant sampling radius of

591 2.5 km. The yellow and blue stars represent the mainshock and the largest aftershock, respectively.

592

593

Figure 3

594 Cross-sections of the b -values in **(a)** period 1 and **(b)** period 2. The yellow and blue stars represent the
595 mainshock and the largest aftershock, respectively. The black circles show the regions where the p -value
596 test was performed. The small black circles represent the events that occurred in each region.

597

598

Figure 4

599 p -values for the regions with different b -values: **(a–d)** period 1; **(e, f)** period 2. N represents the number
600 of events that occurred each region.

601

602

Figure 5

603 **(a, b)** Plan-view b -value maps of the shallow (0.0–9.5 km depth) and deep (9.5–20.0 km depth) regions
604 during period 1. **(c, d)** Plan-view b -value maps of the shallow and deep regions during period 2. The focal
605 mechanisms from the F-net data are superimposed on the b -value maps for the appropriate depth range
606 and time window. The sizes of the focal mechanisms are proportional to their moment magnitudes. The
607 other symbols and meanings are the same as in Fig. 1.

608

609

Figure 6

610 **(a)** Difference in b -values between the first and second periods ($\Delta b = b_{period2} - b_{period1}$) in the shallow
611 region. **(b)** p -values estimated from Δb in (a). **(c)** Difference in b -values in the deep region. **(d)** p -values
612 estimated from Δb in (c). The other symbols and meanings are the same as in Fig. 1.

613

614

Figure 7

615 Stress tensor inversion results for **(a)** period 1 and **(b)** period 2. The large square, triangle, and circle
616 show the best orientations of the maximum, intermediate, and minimum principal stresses, respectively.
617 The small red, green, and blue circles represent the 95% confidence limits of the σ_1 , σ_2 , and σ_3 axis
618 orientations, respectively. The right figures show frequencies of the stress ratios R within the 95%
619 confidence limits.

Figures

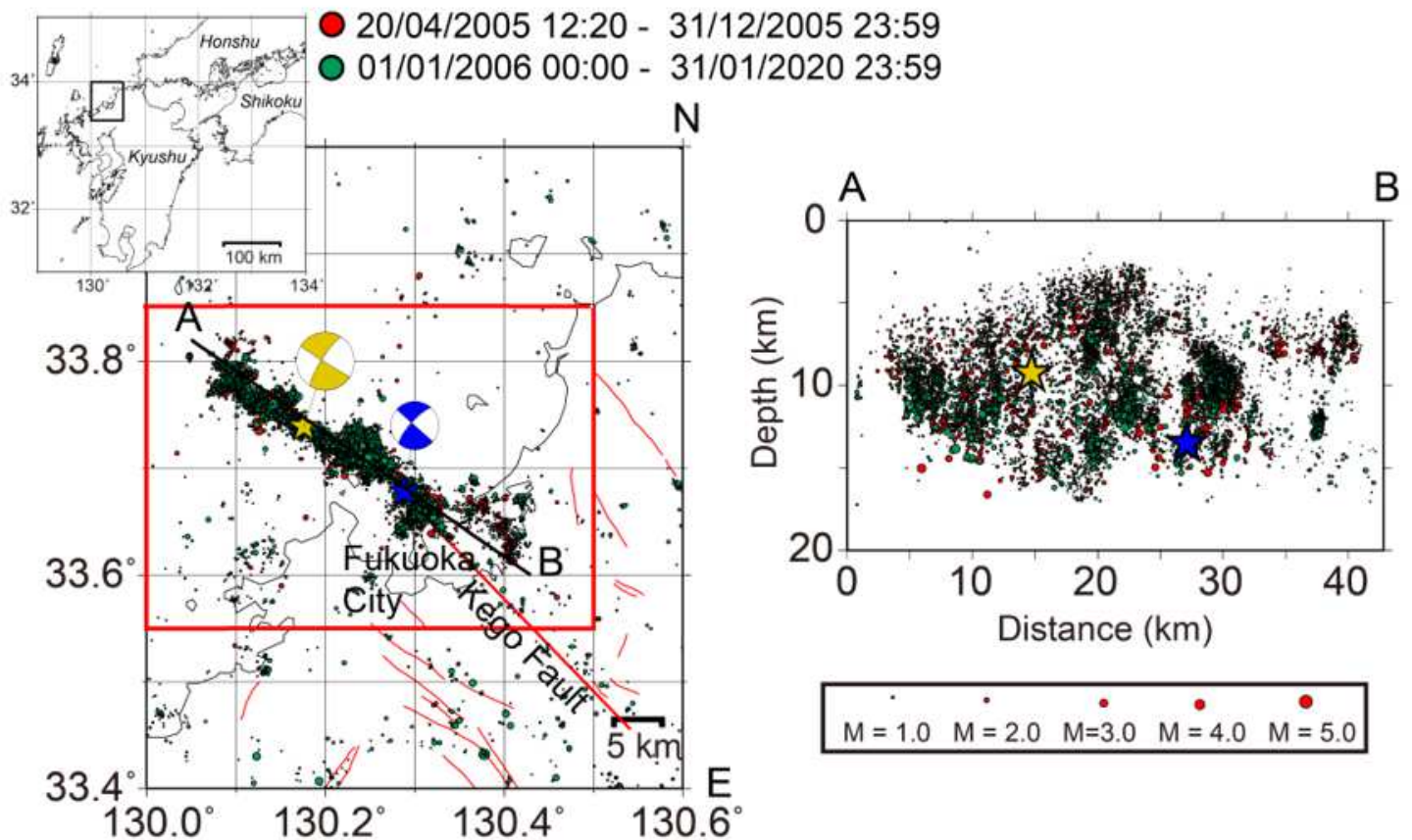


Figure 1

Left: Epicentral distribution of the $M \geq 0.5$ earthquakes. The red and green circles represent the period 1 (12:20 JST on 20 April 2005 to 23:59 on 31 December 2005) and period 2 (00:00 JST on 1 January 2006 to 23:59 on 31 January 2020) events, respectively. The events are scaled by their magnitudes. The yellow and blue stars represent the hypocenters of the mainshock and largest aftershock (MJ 5.8, 06:11 JST on 20 April 2005), respectively. The yellow and blue focal mechanisms are those for the mainshock and largest aftershock, respectively. The red lines indicate active faults (The Research Group for Active Faults of Japan 1991). Line A–B shows the location of the b-value cross-section in Fig. 3. The red rectangle represents the region used for b-value analysis in Figs. 5 and 6. The inset map shows the analyzed region with respect to western Japan. Right: Cross-section of the hypocenters within 5 km of A–B.

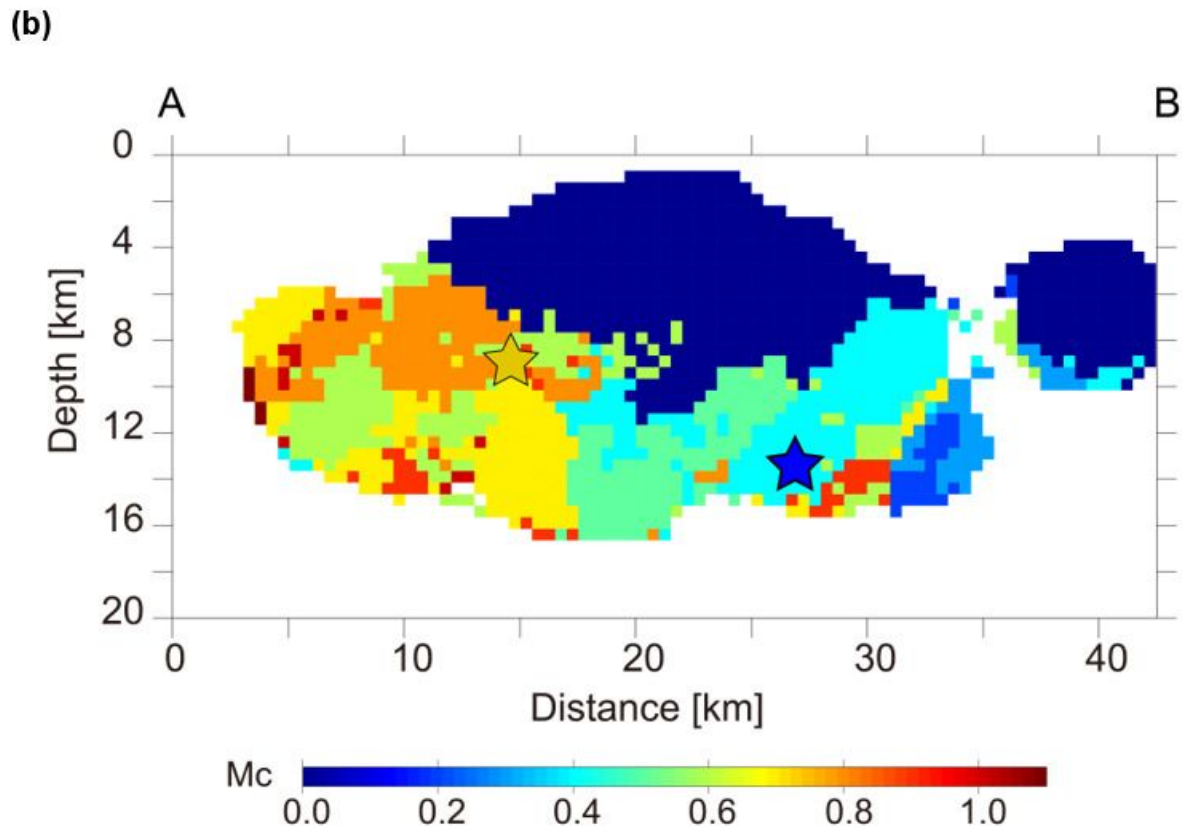
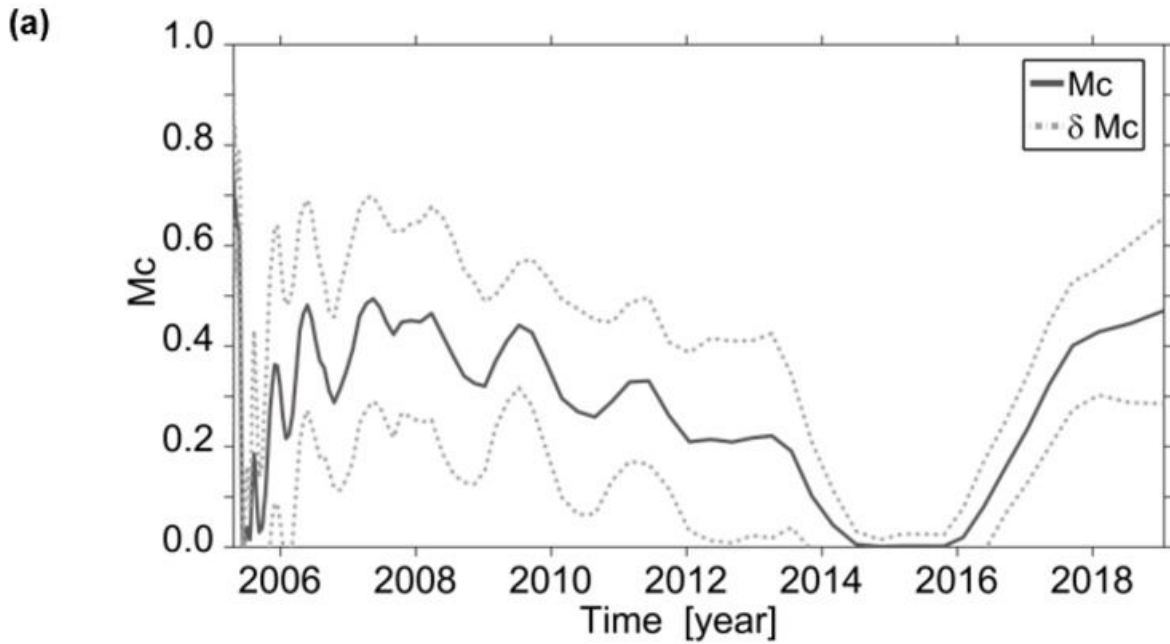


Figure 2

(a) Mc as a function of time in the area bordered by the red rectangle in Fig. 1. The dashed gray lines represent the standard deviation of the calculated Mc values. The maximum curvature method (Wiemer and Wyss 2000) was employed to investigate the Mc distribution in the study area using overlapping 500-event windows and a 20-event step. (b) Spatial distribution of Mc estimated using the maximum

curvature method (Wiemer and Wyss 2000) with 0.5 km grid spacing and a constant sampling radius of 2.5 km. The yellow and blue stars represent the mainshock and the largest aftershock, respectively.

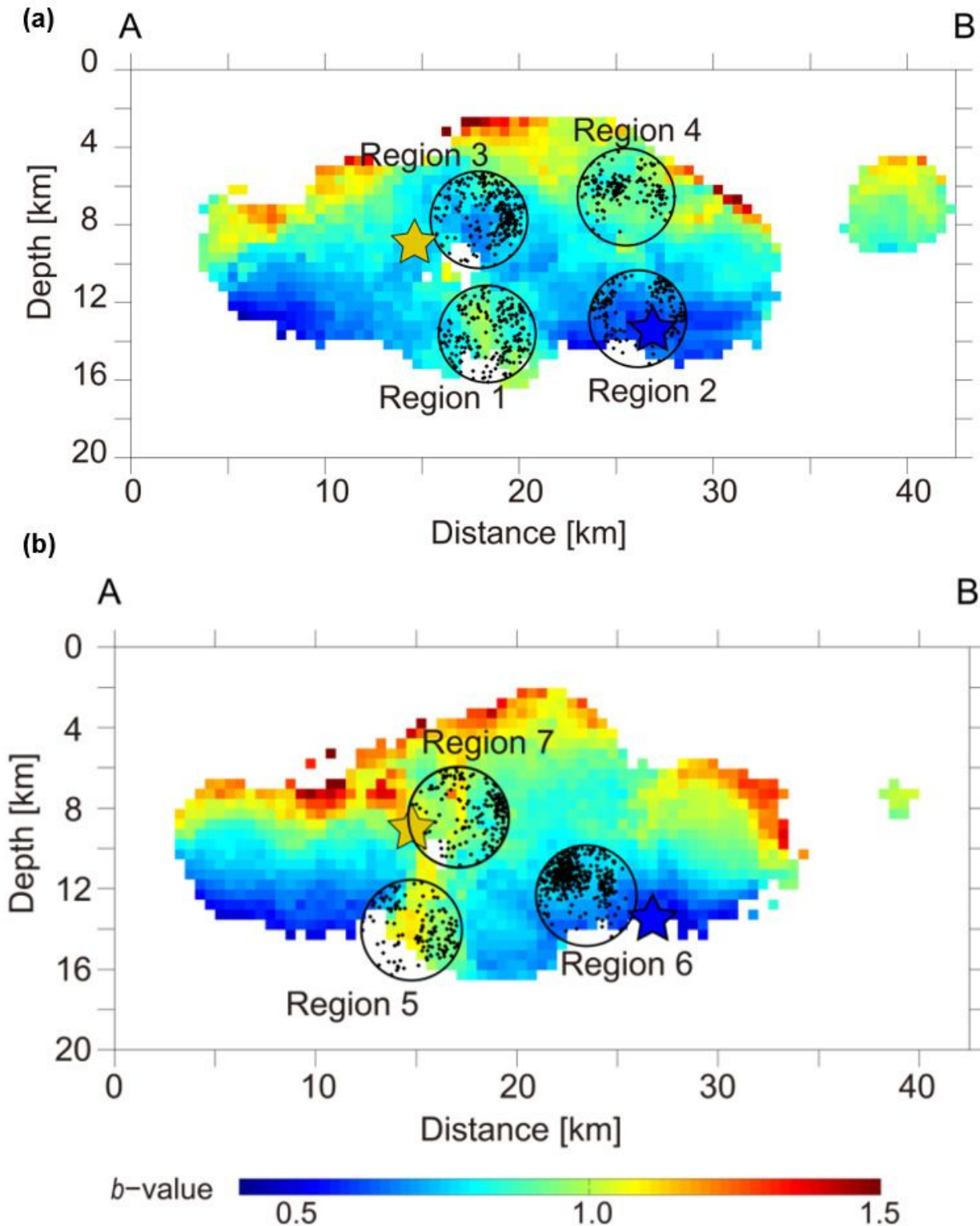


Figure 3

Cross-sections of the b-values in (a) period 1 and (b) period 2. The yellow and blue stars represent the mainshock and the largest aftershock, respectively. The black circles show the regions where the p-value test was performed. The small black circles represent the events that occurred in each region.

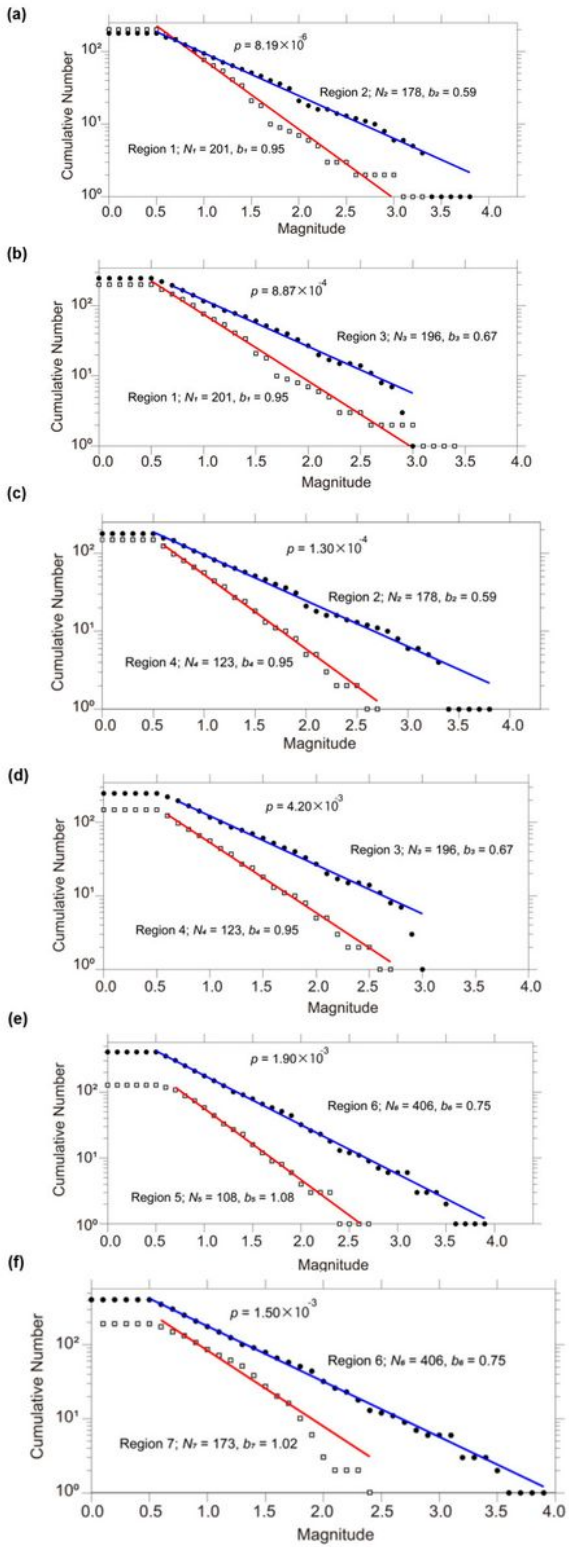


Figure 4

p-values for the regions with different b-values: (a–d) period 1; (e, f) period 2. N represents the number of events that occurred each region.

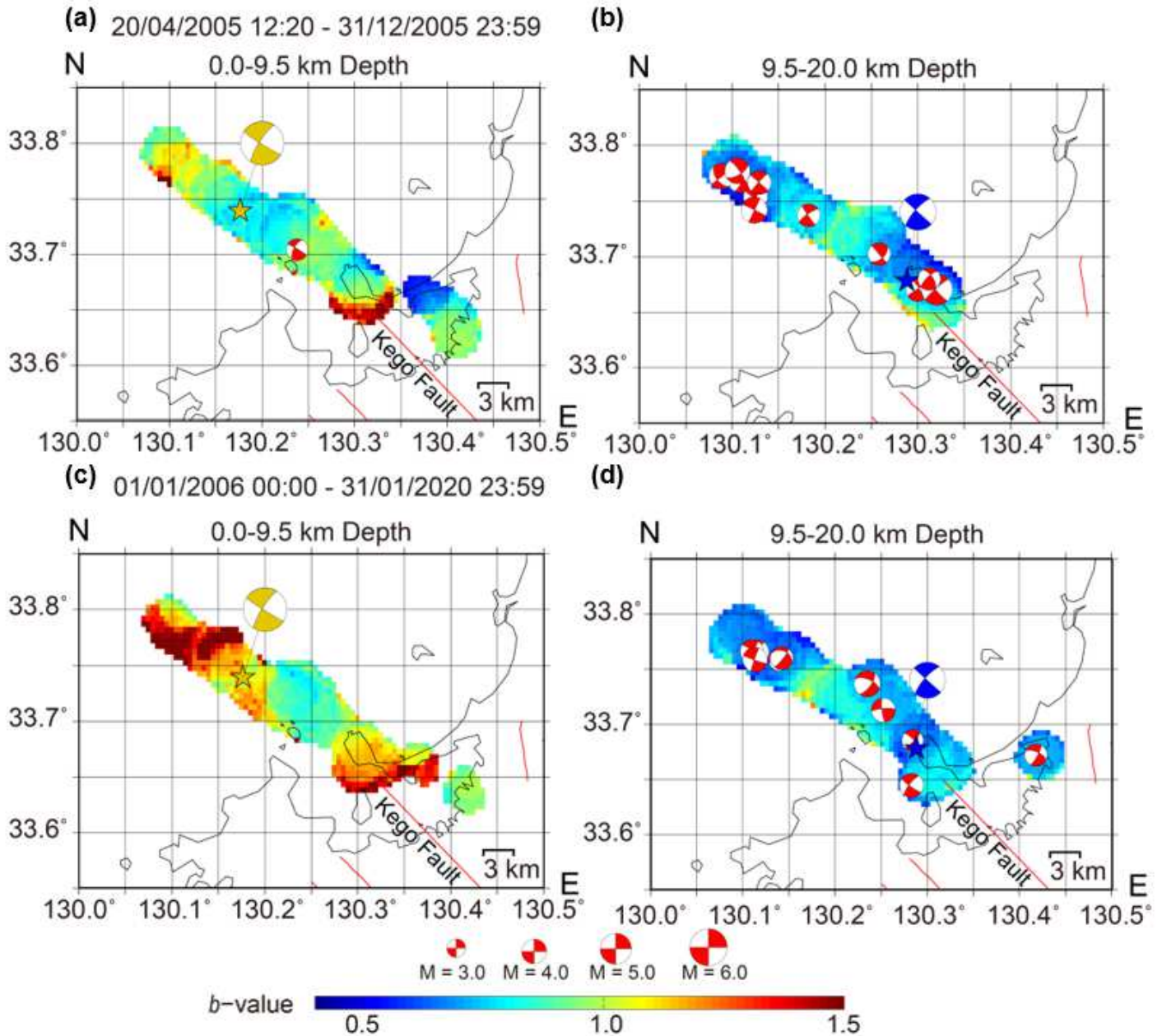


Figure 5

(a, b) Plan-view b-value maps of the shallow (0.0–9.5 km depth) and deep (9.5–20.0 km depth) regions during period 1. (c, d) Plan-view b-value maps of the shallow and deep regions during period 2. The focal mechanisms from the F-net data are superimposed on the b-value maps for the appropriate depth range and time window. The sizes of the focal mechanisms are proportional to their moment magnitudes. The other symbols and meanings are the same as in Fig. 1.

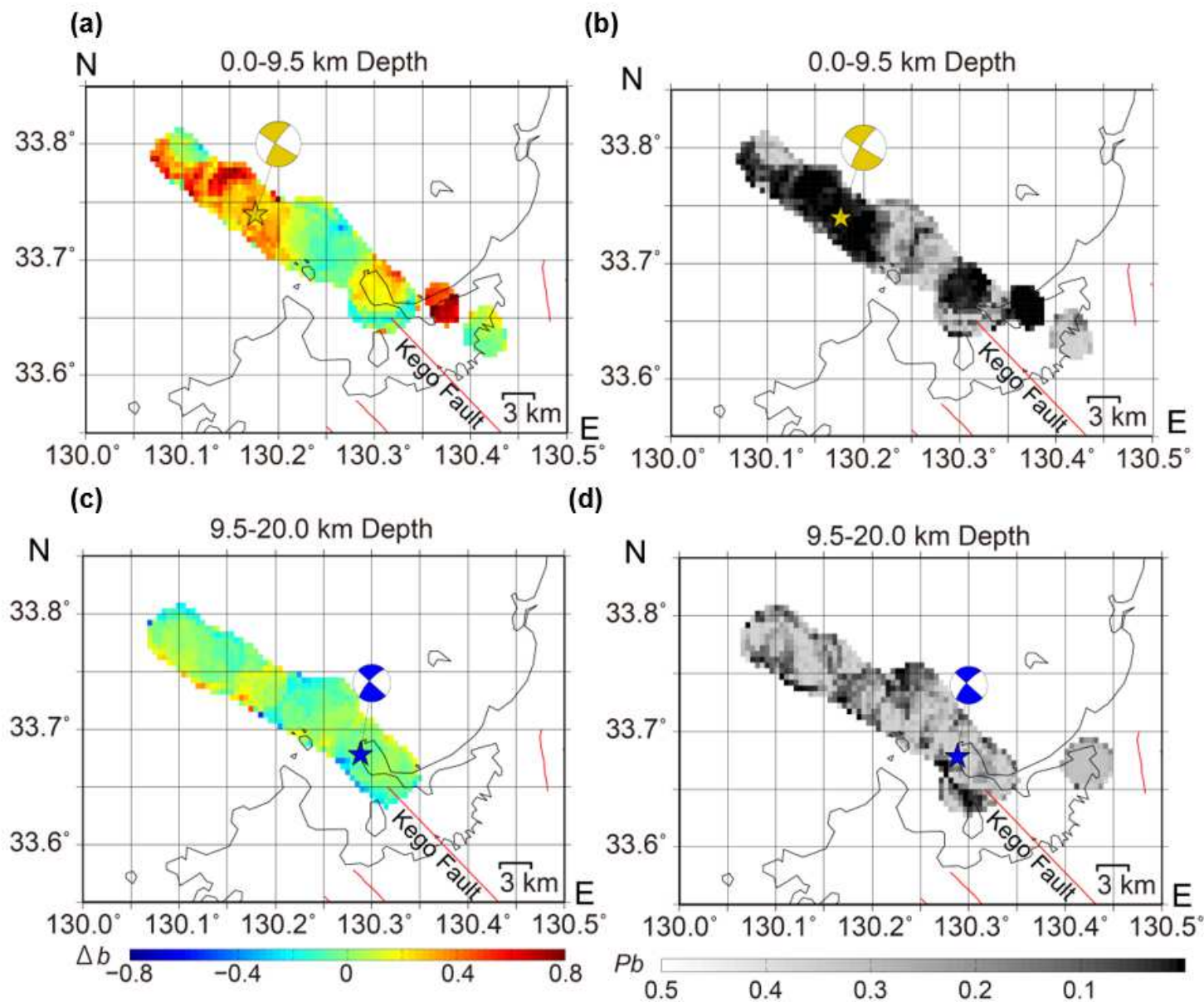


Figure 6

(a) Difference in b-values between the first and second periods ($\Delta b = b_{\text{period2}} - b_{\text{period1}}$) in the shallow region. (b) p-values estimated from Δb in (a). (c) Difference in b-values in the deep region. (d) p-values estimated from Δb in (c). The other symbols and meanings are the same as in Fig. 1.

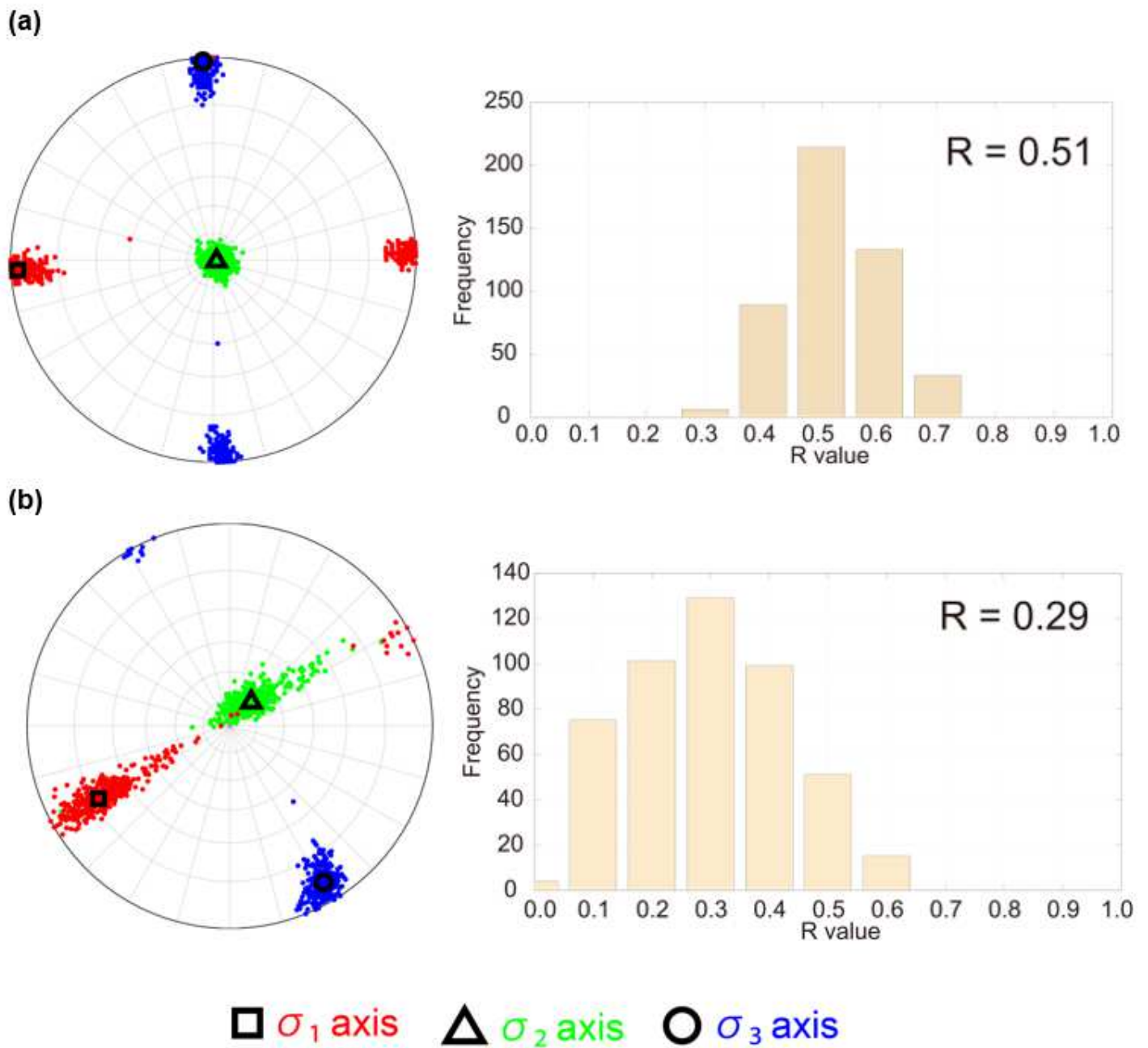


Figure 7

Stress tensor inversion results for (a) period 1 and (b) period 2. The large square, triangle, and circle show the best orientations of the maximum, intermediate, and minimum principal stresses, respectively. The small red, green, and blue circles represent the 95% confidence limits of the σ_1 , σ_2 , and σ_3 axis orientations, respectively. The right figures show frequencies of the stress ratios R within the 95% confidence limits.

Supplementary Files

This is a list of supplementary files associated with this preprint. [Click to download.](#)

- [PAAGD2000347appendixR1.docx](#)